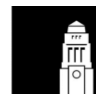
UNIVERSITY OF LEEDS

This is a repository copy of *Resonant tunnelling and intersubband optical properties of ZnO/ZnMgO semiconductor heterostructures: impact of doping and layer structure variation*.

White Rose Research Online URL for this paper:
https://eprints.whiterose.ac.uk/208843/

Version: Accepted Version

Article:
Atić, Aleksandar, Wang, Xizhe, Vuković, Nikola et al. (4 more authors) (Accepted: 2024) Resonant tunnelling and intersubband optical properties of ZnO/ZnMgO semiconductor heterostructures: impact of doping and layer structure variation. Materials. ISSN 1996-1944 (In Press)

This is an author produced version of an article accepted for publication in Materials, made available under the terms of the Creative Commons Attribution License (CC-BY), which permits unrestricted use, distribution and reproduction in any medium, provided the original work is properly cited.

Reuse
This article is distributed under the terms of the Creative Commons Attribution (CC BY) licence. This licence allows you to distribute, remix, tweak, and build upon the work, even commercially, as long as you credit the authors for the original work. More information and the full terms of the licence here: https://creativecommons.org/licenses/

Takedown
If you consider content in White Rose Research Online to be in breach of UK law, please notify us by emailing eprints@whiterose.ac.uk including the URL of the record and the reason for the withdrawal request.

eprints@whiterose.ac.uk
https://eprints.whiterose.ac.uk/

materials

MDPI

Article

Resonant tunnelling and intersubband optical properties of ZnO/ZnMgO semiconductor heterostructures: impact of doping and layer structure variation

Aleksandar Atić [1,2,3], Xizhe Wang [4], Nikola Vuković [1,3], Novak Stanojević [1,5], Aleksandar Demić [4], Dragan Indjin [4] and Jelena Radovanović [1,3,*]

[1] University of Belgrade, School of Electrical Engineering, Bulevar kralja Aleksandra 72, 11120 Belgrade, Serbia; nikolavukovic89@gmail.com (N.V.), radovanovic@etf.bg.ac.rs (J.R.)
[2] Vinča Institute of Nuclear Sciences, National Institute of Republic of Serbia, University of Belgrade, Mike Petrovića Alasa 12-14, 11351 Vinča, Belgrade, Serbia; atic@vin.bg.ac.rs (A.A.)
[3] Centre for light-based research and technologies COHERENCE, Mike Petrovića Alasa 12-14, 11351 Belgrade, Serbia; coherence@vin.bg.ac.rs
[4] School of Electronic and Electrical Engineering, University of Leeds, Woodhouse Lane, Leeds LS2 9JT, United Kingdom; el17xw@leeds.ac.uk(X.W.), D.Indjin@leeds.ac.uk (D.I.), A.Demic@leeds.ac.uk (A.D.)
[5] Vlatacom Institute of High Technologies, Bulevar Milutina Milankovića 5, 11070 Belgrade, Serbia; novak.stanojevic@vlatacom.com (N.S.)
* Correspondence: radovanovic@etf.bg.ac.rs (J.R.)

Abstract: ZnO-based heterostructures are up-and-coming candidates for terahertz (THz) optoelectronic devices, largely owing to their innate material attributes. The significant ZnO LO-phonon energy plays a pivotal role in mitigating thermally induced LO-phonon scattering, potentially significantly elevating the temperature performance of quantum cascade lasers (QCLs). In this work, we calculate the electronic structure and absorption of ZnO/ZnMgO multiple semiconductor quantum wells (MQWs) and current-density - voltage characteristics of non-polar m-plane ZnO/ZnMgO double-barrier resonant tunnelling diodes (RTDs). Both MQWs and RTDs are considered here as two building blocks of a QCL. We show how doping, Mg percentage and layer thickness affect the absorption of MQWs at room temperature. We confirm that in the high doping concentrations regime, a full quantum treatment which includes the depolarization shift effect must be considered, as it shifts mid-infrared absorption peak energy for several tens of meV. Furthermore, we also focus on the performance of RTDs for various parameter changes and conclude that, to maximize the peak-to-valley ratio (PVR), the optimal doping density of the analyzed $ZnO/Zn_{88}Mg_{12}O$ double-barrier RTD should be around 10^{18} cm^{-3}, whilst the optimal barrier thickness should be 1.3 nm with the Mg mole fraction of ~9%.

Keywords: Wide-bandgap oxide semiconductors, resonant tunnelling, intersubband transitions, depolarization shift

Citation: To be added by editorial staff during production.

Academic Editor: Firstname Lastname

Received: date
Revised: date
Accepted: date
Published: date

Copyright: © 2023 by the authors. Submitted for possible open access publication under the terms and conditions of the Creative Commons Attribution (CC BY) license (https://creativecommons.org/licenses/by/4.0/).

1. Introduction

The demand for materials tailored to the mid-infrared (MIR) and terahertz (THz) spectral range is on the rise, leading to a growing number of applications [1–5]. Within these spectrum ranges, semiconductor materials [6–8], especially semiconductor heterostructures and superlattices (SL), present an intriguing avenue for exploring and regulating carrier quantum transport and optical transitions in both radiation sources and detectors [9–17]. In materials science, a SL typically denotes a periodic arrangement of alternating

materials. Following the recent progress in the near-infrared spectral range, semiconductor SL structures hold promise for extending innovative capabilities into the MIR and THz domains [18–23]. Additionally, modern epitaxial growth techniques used in creating quantum-cascade lasers establish a highly competitive technology for the MIR and THz range [24–26].

Furthermore, the study of linear and nonlinear optical properties in quantum heterostructures like SLs and quantum wells based on wide bandgap oxide semiconductors are in focus due to their potential applications in optoelectronics, such as QCLs [1,27–29] and RTDs [30]. The properties of these devices are based on two quantum phenomena: electronic confinement and tunnelling. Intersubband transitions (ISBT) are typically collective effects that involve large electron densities of interacting particles and the most important manifestation of this collective character is that, in the presence of electromagnetic radiation, each electron is affected by an effective field induced by the excitation of the other electrons, called a depolarisation field [31,32].

GaAs-based QCLs are the most promising devices emitting in the terahertz frequency range, but they lack significant improvements within recent years and are still limited to operation at low temperatures (~260K) [33]. They are fundamentally limited by electron-optical longitudinal optical (LO)-phonon resonance at around 36 meV in GaAs, causing parasitic non-radiative depopulation of the upper laser level at room temperature. The 260 K record performance has been established due to a paradigm shift in designing structures beyond LO-phonon resonance energy [34,35], however, the fundamental limit lies in nonradiative electron - LO-phonon scattering between the lasing levels [35] and this can only be mitigated by using material systems with larger resonant LO-phonon energy. Promising alternative semiconductors to solve this problem include new material systems like zinc-oxides (ZnO) with their larger LO-phonon energy (~72meV) [27]. ZnO with a hexagonal wurtzite structure is currently emerging as a promising II-VI direct wide bandgap semiconductor for its use in photonic devices such as LED, solar cells, thin film transistors and other heterostructures [36–39]. High resonant electron LO-phonon energy in ZnO-based compounds is just one important beneficial property, and their large bandgap, high conduction band offset and resistance to electric breakdown are other relevant benefits [39–45]. Furthermore, prospective ZnO-based lasers can cover a 5-12 THz emission frequency range [46], an important range relevant for the detection and imaging of explosives, which cannot be covered by standard GaAs-based THz QCLs. Recently achieved progress in the growth of low-density defect non-polar m-plane ZnO-based heterostructures [47] opens a perspective towards the demonstration of ZnO-based unipolar structures capable of operation at elevated or even room temperature.

Sizeable optical phonon energy in ZnO-based structures should facilitate the population inversion for ISBTs with energy well below the optical phonon energy [47]. Despite significant advances in the reproducibility and the stability of the p-doping of ZnO, it remains a considerable challenge, which strongly limits the development of this wide bandgap oxide semiconductor for bipolar electrical devices [47]. Still, it may be possible to use ZnO-based heterostructures for unipolar devices (with only n-type doping) such as RTDs, quantum well-infrared photodetectors, quantum cascade detectors or lasers [47]. To master the fabrication of ZnO-based quantum cascade structures, a high-quality epitaxial growth is crucial, combined with a well-controlled fabrication process including (selective) Zn(Mg)O etching and the deposition of low-resistance ohmic contacts. V. Sirkeli et al. report a numerical study of negative differential resistance in non-polar m-plane ZnO/ZnMgO THz RTDs with double and triple quantum barriers [48]. They show that by optimising the design structure of RTDs, the constituent layer material, its width, and doping level, the mW-level output power of terahertz emission from these

devices could be achieved at room temperature [48]. Liu et al. investigated THz intersubband absorption in step quantum well structures based on ZnO/ZnMgO materials at 77 K [49]. Recently Meng et al, have demonstrated the first intersubband electroluminescence from non-polar m-plane ZnO QC structures [37].

In this paper, we numerically investigate the different combinations of ZnO/ZnMgO multi-quantum well and resonant-tunnelling structures to analyse the sensitivity of the position and magnitude of intersubband absorption peak and the tunnelling current peak-to-valley ratio on monolayer-scale layer structure, Mg composition fluctuation, and doping density variation.

2. Methods

We start from the one-dimensional envelope function effective-mass Schrödinger equation:

$$-\frac{\hbar^2}{2}\frac{d}{dz}\frac{1}{m^*(z)}\frac{d\psi_i(z)}{dz}+U_{eff}(z)\psi_i(z)=E\psi_i(z), \quad (1)$$

Where $\psi_i(z)$ is the envelope wave function, E is the eigenvalue of electron energy, m^* is the electron's effective mass, and $U_{eff}(z)$ is the total effective potential energy given as:

$$U_{eff}(z)= U_c(z)-e\varphi(z)+U_{xc}(z)-eFz \quad (2)$$

where U_c is the conduction band edge of the heterostructure, F is the externally applied electric field, and $\varphi(z)$ is electrostatic potential. U_{xc} is the local exchange-correlation potential described in Appendix A. ZnO bandstructure indicates very high neighbouring valleys as illustrated, for example, in [50] where the higher valley minima would be ~1.5-2 eV above the G valley, thus we expect no or very small band-mixing effects. Therefore, the use of a single-band envelope function effective-mass model here is justified.

The total effective potential energy depends on the envelope functions in a semiconductor heterostructure, and the system of Schrödinger-Poisson equations needs to be solved self-consistently. The electrostatic potential of the Poisson equation reads:

$$\frac{d^2\varphi(z)}{dz^2}=\frac{e}{\varepsilon(z)}\left(n(z)-N_D(z)\right), \quad (3)$$

where, as above, $\varphi(z)$ is the electrostatic potential, $\varepsilon(z)$ is the dielectric constant, and $N_D(z)$ is the doping concentration. In a semiconductor MQW-based heterostructure bound electron energies can, therefore, be calculated fully quantum mechanically, and the electron density $n(z)$ is given as:

$$n(z)=\sum_i N_{s,i}|\psi_i(z)|^2, \quad (4)$$

where $N_{s,i}$ is the sheet carrier density corresponding to the i-th electron bound state defined as:

$$N_{s,i}=\frac{m_{ti}k_BT}{\pi\hbar^2}\ln\left(1+e^{\frac{E_F-E_i(0)}{k_BT}}\right). \quad (5)$$

In the above eq. E_F is the Fermi energy, $E_i(0)$ is the quasi-bound state energy for zero transversal wave vector $(k_t = 0)$, k_B is the Boltzmann constant, and T is the crystal lattice absolute temperature. m_{ti} is the transversal mass defined as:

$$\frac{1}{m_{ti}} = \int \psi_i^*(k_t = 0)\frac{1}{m^*(z)}\psi_i(k_t = 0)dz. \quad (6)$$

In finite gap semiconductors, non-parabolicity is typically characterised by energy-dependent effective mass [51,52]. It is taken as a weak effect here as it must be sufficiently close to the band edge with a finite gap. The material system that we consider in this work has a wide energy gap, thus, the band nonparabolicity can be neglected.

In quantum heterostructures based on potential barriers like resonant tunnelling structures, all electron energy levels belong to a continual spectrum, and the resonant electron states can be quantified by tunnelling coefficient $\tau(E)$. If the electric field (terminal voltage) F is applied across the structure, the current density can be calculated using the Esaki-Tsu formula [53]. This simplified approach assumes a coherent picture of electron tunnelling, using the approximation that electron transport is not affected by any phase-coherence-breaking scattering effects [54]. This carrier transport model has been commonly used to characterise resonant tunnelling structures based on different material systems [54–56]. Based on these assumptions, the current density in the tunnelling structure can be calculated as follows:

$$J = \frac{ek_BT}{2\pi^2\hbar^3}\int_{E_c}^{\infty} m^*\tau(E)\ln\left[\frac{1+e^{\frac{E_F-E}{k_BT}}}{1+e^{\frac{E_F-E-eV_R}{k_BT}}}\right]dE \quad (7)$$

where for the reference level $E_c = 0$ conduction band minima can be used, $\tau(E)$ is the transmission (tunnelling) coefficient, E_F is the Fermi energy in the highly doped emitter of resonant tunnelling structure, V_R is the potential drop across the structure (such that $V_R = F \times lenght\ of\ resonant\ structure$) and m^* is the effective mass in well material. The Fermi energy E_F is calculated here using Fermi-Dirac statistics in a highly doped emitter/collector assuming that all donors are ionised, i.e. that electron concentration in the emitter/collector is $n = N_D$ [57]. The magnitude of the current density (obtained from this coherent electron transport model) does not take into account other contributing factors to the total current, such as the scattering current and the thermionic current, thus only the relative trends in carrier transport and possible negative differential resistivity behaviour can be identified and predicted in a prospective experiment. We can also express the electron density in the resonant tunnelling structure as [54,56]:

$$n(z) = \frac{k_BT}{2^{\frac{3}{2}}\pi^2\hbar^3}\int_{E_c}^{\infty}|\psi(z,E)|^2\,(m^*)^{\frac{3}{2}}E^{-\frac{1}{2}}\ln\left[1+e^{\frac{(E_F-E)}{k_BT}}\right]dE + \frac{k_BT}{2^{\frac{3}{2}}\pi^2\hbar^3}\int_{E_c-eV_R}^{\infty}|\psi(z,E)|^2\,(m^*)^{\frac{3}{2}}E^{-\frac{1}{2}}\ln\left[1+e^{\frac{(E_F-E-eV_R)}{k_BT}}\right]dE \quad (8)$$

In a multi-quantum-well-based structure, the sub-barrier energy spectre, in a good approximation, can be assumed as discrete. The energies and wave functions of the bound states found from the Schrödinger-Poisson solver are further used to calculate optical absorption $A(\omega\hbar)$ for the intersubband transitions. In the single-particle picture, the absorption coefficient is [32]:

$$\alpha_{2D,s}(\omega) = C_s\sum_{\alpha} f_\alpha\Delta N_\alpha L(\omega-\omega_\alpha), \quad (9)$$

Where C_s is a constant, f_α is the oscillator strength of the transition α and $L(\omega - \omega_\alpha)$ is a Lorentzian centred in the intersubband transition frequency ω_α.

In a situation when a single subband is occupied, a blue shift of the absorption peak is observed (relative to the transition frequency), corresponding to the excitation of a collective mode of the system called the intersubband plasmon [32]. In case when confined levels in the QW are closely spaced together and more than one of them is populated by electrons, several intersubband transitions occur simultaneously, resulting in the optical spectrum which consists of a single resonance whose energy is entirely different in comparison with the bare intersubband transitions. The resonance corresponds to the excitation of a collective mode of the system, the multisubband plasmon, resulting from the phase locking of all different intersubband transitions. Multisubband plasmons have been the subject of intense research in the last decade [58] and have proven to be an excellent platform for investigating the ultrastrong coupling of light and matter excitations in an optical cavity. Multisubband plasmon can be imagined as a charge density wave where the collective dipole oscillates along the growth direction of the quantum well (z-axis), while the plasmon propagates in the quantum well plane (x-y plane), with a characteristic in-plane wavevector [59].

The absorption coefficient can be calculated by integrating all the current densities associated with different multisubband plasmons (see Appendix B):

$$\alpha_{2D,m}(\omega) = C_m \sum_n \frac{1}{W_n} \left| \int_{-\infty}^{+\infty} J_n(z) dz \right|^2 L(\omega - W_n)$$
$$= C_m \sum_n W_n F_n \, L(\omega - W_n), \quad (10)$$

where C_m is a constant, $W_n F_n$ is the effective oscillator strength for n-th multisubband plasmon mode, and L is Lorentzian (or Gaussian) centred at the multisubband plasmon frequency W_n. Each effective oscillator strength results from the contribution of all the optically active intersubband plasmons. They are weighted by different quantities associated with individual transitions, such as dipole matrix elements or transition frequencies. They also depend on the coupling between intersubband plasmons, which enters through the eigenvectors of the matrix M. The coupling between intersubband plasmons results in a redistribution of the absorption amplitude from the intersubband transitions to the multisubband plasmon modes. The total absorption satisfies the conservation of the total transition probability:

$$\sum_\alpha \omega_\alpha |z_\alpha|^2 \, \Delta N_\alpha = \sum_n W_n F_n. \quad (11)$$

where z_α represents a dipole matrix element of the transition α.

3. Results and Discussion.

3.1. Multiple quantum well structure

In the first part of this section, we show results for ISBT optical absorption simulation in the multiple QW structure analogues to the structure introduced in [46] which could serve as a period of a QCL active region. The well material is ZnO, while the barrier material is $Zn_{88}Mg_{12}O$. The structure was grown on a nonpolar m-plane ZnO substrate. The appearance of cracks in an epitaxial layer grown on a mismatched substrate - as (Zn, Mg)O on ZnO - can be predicted using the critical thickness criteria as in the reference

[60]. The critical thickness is defined as the maximum thickness that can be grown before the nucleation of the first crack in the layer. It turns out that for the THz cascade devices samples (which have a low Mg content range), relaxation on the m-plane is not a problem because the critical thickness for 15% of Mg is above 1 μm, which allows the growth of THz cascade devices made from m-plane ZnO and (Zn, Mg)O without defects. On the other hand, the realization of QCL in the IR range using the m-plane is not possible because the Mg content is higher and consequently the critical thickness is greatly reduced.

The temperature of *T*=*300* K, and the operating external electric field $F = 73 \frac{kV}{cm}$. were set in all simulations. Figure 1 shows the conduction band diagram of the structure. The effective mass in the well and barrier is taken as equal, and it reads $m^* = 0.28m_0$. The effective masses of the QWs and the barriers were taken to be the same as that of ZnO polaron mass as in [61], due to the strong interaction between electrons and phonons in this highly ionic material. The assumption of equal effective masses in the well and barrier does not introduce a significant error since the Mg content has been taken around 12% to lead to a conduction band offset of ~200meV.

Conduction band offset is calculated as $\Delta E_c = 0.675\Delta E_g$ [61,62], where ΔE_g is the difference in band gap between the two semiconductors in the junction and is calculated as 25 meV multiplied by % of Mg in the barrier.

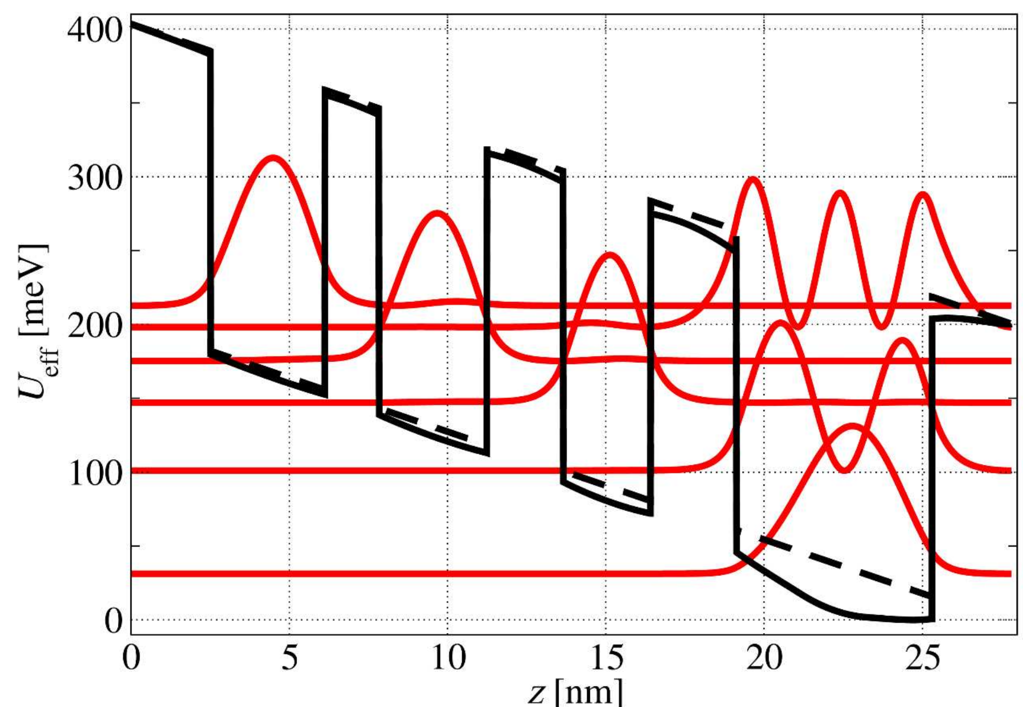

Figure 1. Conduction-band diagram of ZnO/Zn88Mg12O multiple QW structure in an applied electric field. The layer sequence of the structure in nanometers from the left to the right is **2.5**/3.6/**1.7**/3.4/**2.4**/2.75/**2.7**/<u>6.15</u>/**2.5,** where the barriers are in bold, while regular characters are ZnO wells. The centre (2.05 nm) of the 6.15nm well (underlined) is doped with Ga to $N_D = 3 \times 10^{18}$ cm^{-3}. Bound states and their corresponding wave functions squared are denoted with full red lines. The dashed black line shows the effective potential energy without the effect of the well doping.

Figure 2 shows that the calculated absorption peak for moderate Ga doping values ($N_D = 3 \times 10^{18}$ cm^{-3}) is around 70 meV. The difference between the single and multi-subband plasmon pictures is only a couple of meV. Comparatively, for the large values of

Ga doping ($N_D = 5 \times 10^{19}$ cm^{-3}), we notice that in a single plasmon picture, the absorption peak is around 100 meV while in multisubband plasmon picture, the peak is around 170 meV, which represents a significant difference showing that the effect of the depolarisation shift cannot be disregarded. The more we increase the doping, the more pronounced the depolarisation shift becomes. This is also illustrated in Figure 3. in which the energy corresponding to the absorption peak is plotted as a function of doping density. The Inset of Figure 3. shows the dependence of the absorption coefficient on doping density.

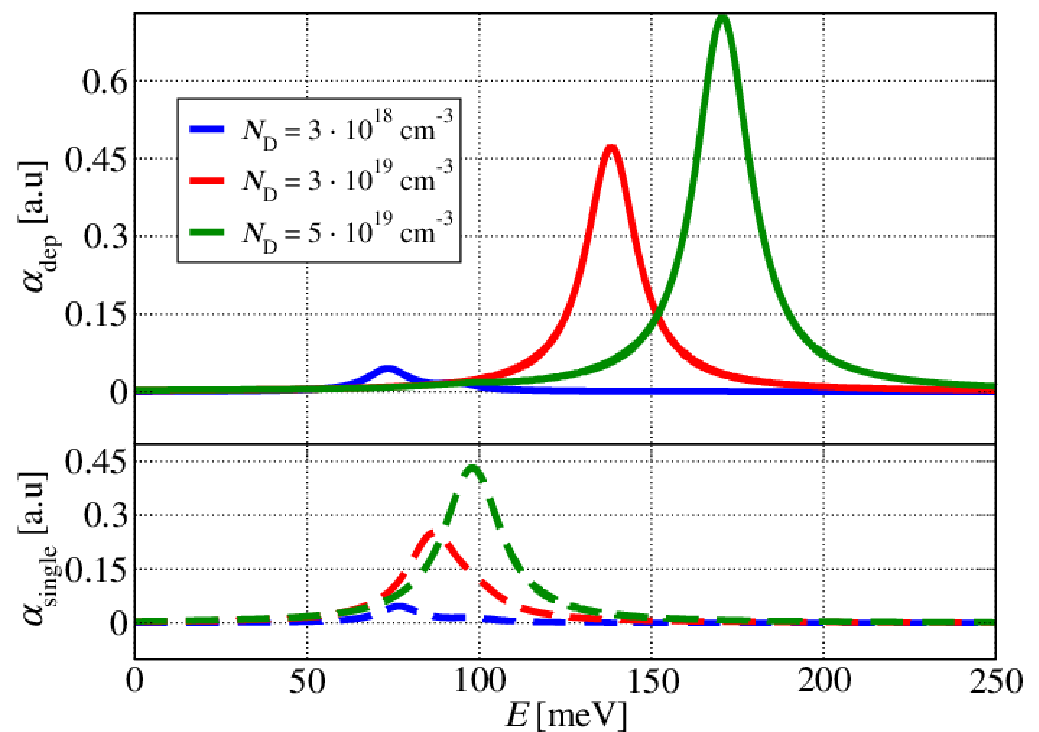

Figure 2. Intersubband absorption spectra for differing values of the wide well doping in the structure from Figure 1. The upper diagram shows the absorption spectra with depolarisation shift, while the lower one shows the absorption spectra calculated in a single plasmon picture.

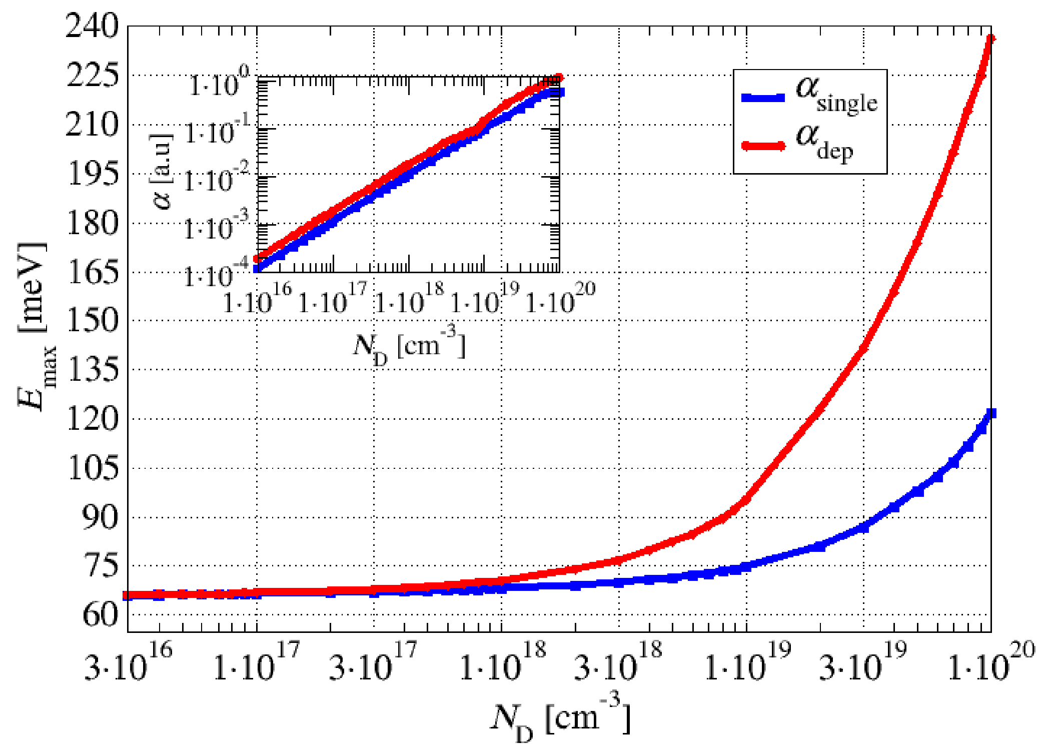

279

Figure 3. Absorption peak energy as a function of the wide well doping density in the structure given in Figure 1. The blue line denotes a single plasmon picture, while the red line shows the results of a full quantum treatment which is necessary for higher doping concentrations. Inset shows the absorption coefficient peak magnitude change as a function of wide well doping. 280 281 282 283

In Figures 4. and 5. we show calculated absorption for the large doping concentration $N_D = 5 \times 10^{19}$ cm^{-3} accounting for the depolarisation field i.e. in the full multisubband plasmon picture. The change in the conduction band offset (CBO) by sweeping the percentage of Mg in the barrier layers from 10% to 14% with a 1% increment, results in the shift in the absorption spectra shown in Figure 4. The absorption peak energy redshifts as the Mg percentage in the barrier increases. The impact of the slight variations of the width of the doped well by ±2.5Å steps on the absorption spectra is shown in Fig. 5. Increasing the well width blue-shifts the absorption spectra. 284 285 286 287 288 289 290 291

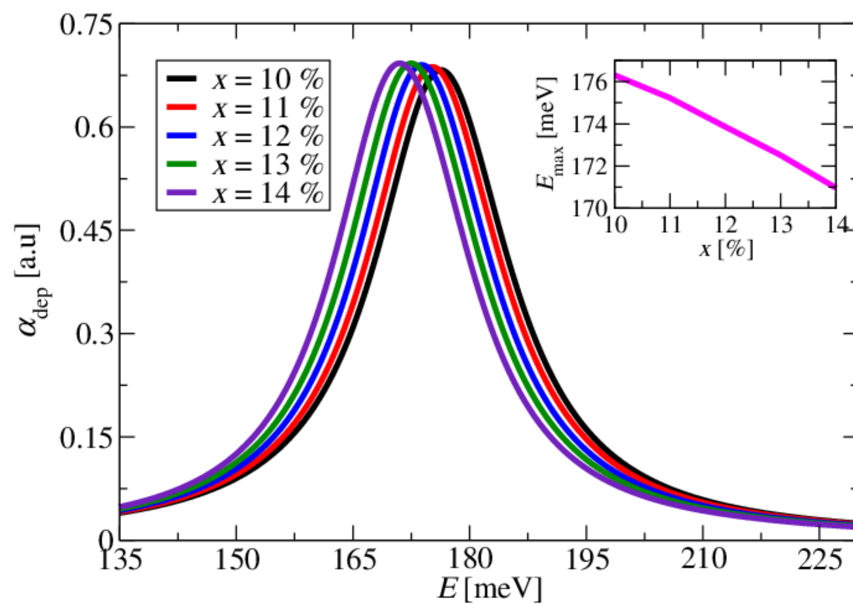

292

Figure 4. Absorption spectra for differing values of Mg composition in barrier layers. The doping density of the wide well is set to $5 \times 10^{19}\ cm^{-3}$, and a lattice temperature of T=300K is used in all simulations. Inset shows the energy that corresponds to the absorption spectrum peak position as a function of Mg composition in barrier layers. As the percentage of Mg increases, the absorption spectrum peak is red-shifted by approximately 5meV. 293 294 295 296 297

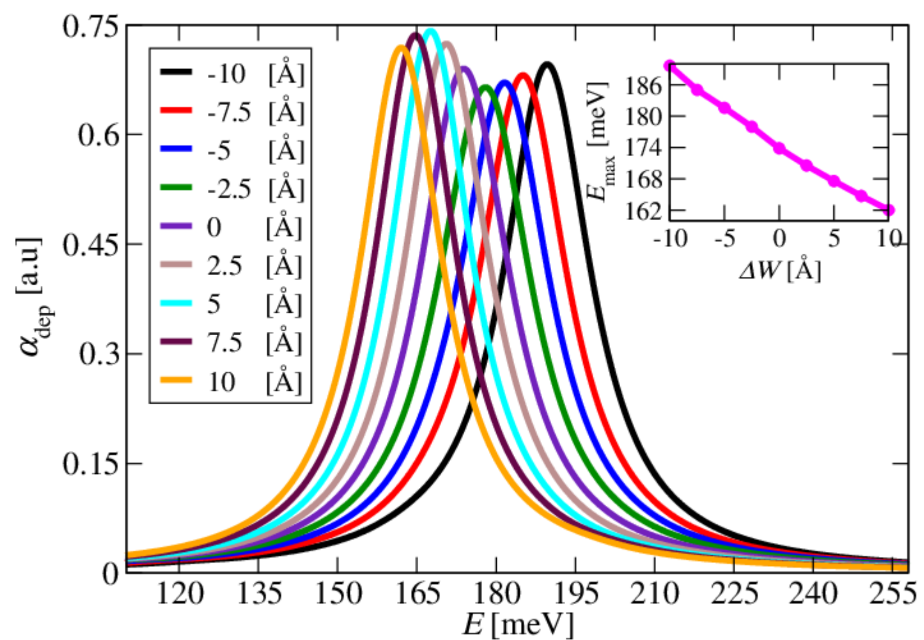

298

Figure 5. Figure shows that an expansion of the well width red-shifts the absorption spectra. The inset shows the absorption peak energy as a function of the change of the well width ΔW. 299 300

3.2. Resonant tunnelling structures

In this subsection, we focus on the resonant tunnelling structures. In the first set of calculations, we analyse a non-polar m-plane ZnO/ZnMgO double barrier resonant tunnelling structure in order to investigate the effect of layer thickness fluctuation and the impact of doping density variation on the resonant tunnelling performance of the structure. The first analysed structure has a 6 nm thick ZnO quantum well surrounded by two $Zn_{88}Mg_{12}O$ barriers, each 2 nm thick. The layer thicknesses and Mg composition in barrier layers have been chosen to mimic the resonant tunnelling (electron injection) part of the prospective quantum-cascade structure. The double barrier structure was placed between the injector and collector ZnO layers and the external bias V_R in the range between 0 and 0.25V is applied to this short structure. The Ga doping of the injector/collector was set to be $N_D = 3 \times 10^{18}$ cm^{-3}. Self-consistent effective potential and corresponding electron concentration at lattice temperature of T=300K for three different biasing conditions are shown in Fig. 6. It can be seen that the conduction-band edge at the centre of the quantum well is bent upwards due to the increased electron population in the lowest quasi-bound level at lower voltages as it is closer to the Fermi energy in the highly doped emitter side. Thus, the larger electron concentration in the quantum well gives rise to a stronger self-consistent field resulting in larger band bending. For the larger applied voltages (for example $V_R = 0.15$ V in Fig. 6) the curvature of self-consistent electron concentration in the well region changed its shape as the effective potential in the well region drops down i.e. second quasi-bound state in the well region accumulates electrons and becomes relevant for the carrier tunnelling process.

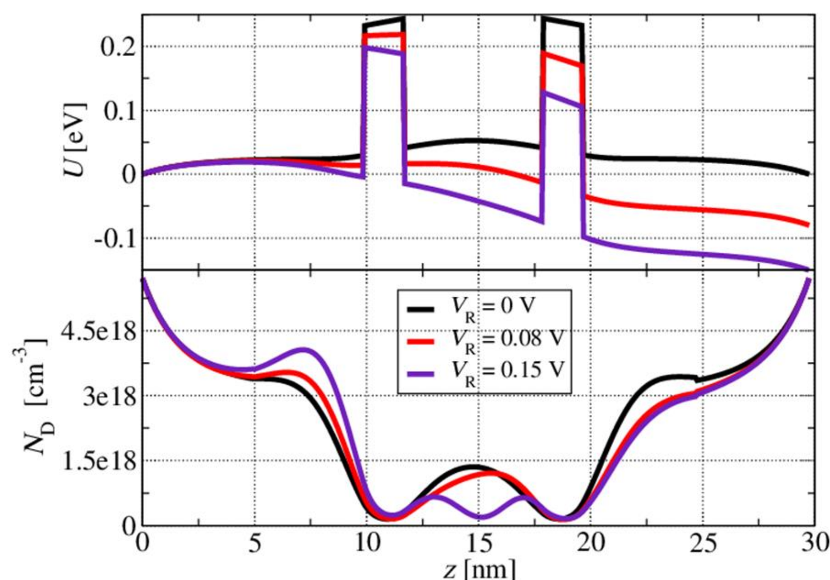

Figure 6. Self-consistent potential and corresponding electron concentration for three different biasing conditions.

In the second set of calculations, the emitter and collector region doping of the m-plane ZnO-based double barrier resonant tunnelling structure is varied from 10^{17} cm^{-3} to 5×10^{18} cm^{-3}. For all simulations, the lattice temperature was again set to T=300 K. Figure 7. shows the current density-voltage characteristics of the structure for three values of doping. The current density increases with the increasing doping level

of the emitter and collector over the whole range of bias voltages. Figure 7. also shows that for all investigated dopings current density-voltage curves have a region with negative differential resistance (NDR).

The peak-to-valley ratio is the ratio between the local maxima and the local minima around the NDR points in RTD's current-voltage (*I-V*) characteristic. Nominally, RTD can have multiple resonances depending on the design of electron subband states, in practical cases, the most important is the first "hump" in *I-V*. Another important metric for RTDs is also the dynamic range that mathematically is the difference between these current values rather than their ratio. Depending on the application, the dynamic range may be also a very important figure of merit for RTD's performance. From the insets in Figure 7. one can see that the current density peak-to-valley ratio (indicates the quality of peak separation), a peak-to-valley difference of current density ΔJ at NDR, and voltage value V_{NDR} at the NDR region, depend on the doping level of emitter and collector. The PVR is increased with increasing the doping level of the emitter and collector and has a maximum PVR of ~ 1.255 at the doping concentration of $10^{18}\ \mathrm{cm}^{-3}$. Further increase of the doping level of emitter and collector leads to the decrease of PVR, and at the doping concentration above $5\times10^{18}\ \mathrm{cm}^{-3}$, the region with NDR feature has almost disappeared (PVR~1). From these results, it can be anticipated that an optimal n-type doping level of the emitter and collector of this structure is around $10^{18}\ \mathrm{cm}^{-3}$.

As pointed out earlier, ZnO/ZnMgO material system has attracted much interest in recent times even though the crystal growth of this system is technologically challenging. Furthermore, layer thickness variation and interface roughness on the order of a fraction of a monolayer is another issue that arises [63]. Structures based on resonant tunnelling mechanisms like THz QCLs [46] require high quality and very precise growth of the layer structures to provide efficient electron resonant tunnelling and a selective injection transport process into the upper laser level. To analyse the impact of layer thickness fluctuation in the ZnO/$Zn_{88}Mg_{12}O$ resonant tunnelling structure, we have performed one more set of the current-density - voltage characteristics simulations in a reference double-barrier resonant tunnelling structure with nominal barrier thickness of around 2 nm and well thickness of 6 nm. This structure is similar and mimics the resonant injection layers in the THz quantum-cascade structure of Ref [46]. The doping density value of $3\times10^{18}\ \mathrm{cm}^{-3}$ in emitter and collector regions at a temperature of T=300 K are used in simulations. As shown in Figure 8., monolayer fluctuation of $Zn_{88}Mg_{12}O$ barrier thickness W_B, despite its relatively low Mg composition, would produce an important impact on the magnitude of the tunnelling current, PVR and current-density peak-to-valley difference, indicating itself as an important parameter in prospective ZnO/ZnMgO THz QCL electron transport optimisation. The Inset of Figure 8. shows that an optimal value of around 1.3 nm has been predicted for this particular resonant tunnelling structure.

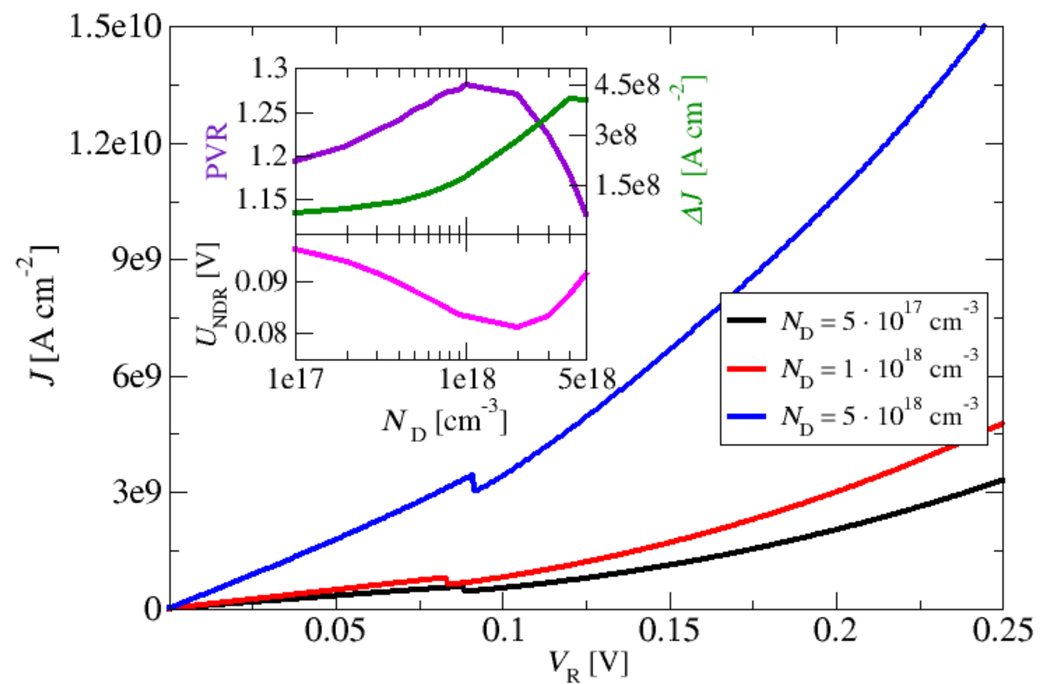

371

Figure 7. Current-density - voltage characteristics of non-polar m-plane ZnO/$Zn_{88}Mg_{12}O$ resonant tunnelling structures. The doping level of the emitter and collector on the current density varied in the range from $10^{17}\ cm^{-3}$ to $5 \times 10^{18}\ cm^{-3}$. The layer thickness barriers and quantum wells of constituent epi-layers of the structure starting from the emitter in nm are 10/**2**/6/**2**/10 (thickness of quantum barriers are marked in bold). Inset shows the current-density peak-to-valley ratio (upper panel left-hand y-axis) and current-density peak-to-valley difference (upper panel right-hand y-axis) at NDR; NDR voltage as a function of the emitter is shown in the lower panel inset. 372 373 374 375 376 377 378

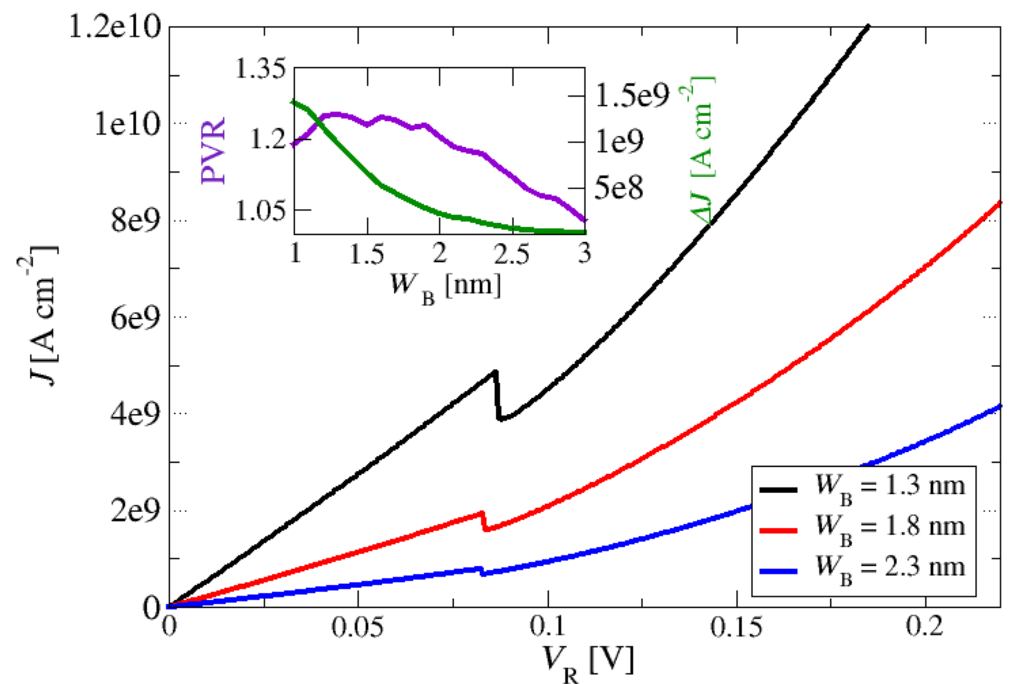

379

Figure 8. Current-density - voltage characteristics of non-polar m-plane ZnO/$Zn_{88}Mg_{12}O$ double-barrier resonant tunnelling structures. The thickness of barriers W_B have been exposed to monolayer-scale fluctuation around a nominal value of 2 nm. The nominal layer thicknesses barriers and quantum well of constituent epi-layers of the structure starting from the emitter in nm are 380 381 382 383

10/**1-3**/6/**1-3**/10 (thickness of quantum barriers are marked in bold). Inset shows the current-density peak-to-valley (PVR) ratio (left-hand y-axis) and current-density peak-to-valley difference (right-hand y-axis) at NDR; Doping density value in emitter/collector of $3 \times 10^{18}\ cm^{-3}$ and lattice temperature of T=300K is used in all simulations.

Finally, in order o to analyse the impact of Mg mole fraction variation in an RTD with (previously obtained) optimised doping density of N_D=1×$\mathbf{10^{18}\ cm^{-3}}$ and barrier thickness of W_B=1.3 nm, we have performed the final set of the current-density-voltage characteristics simulations. As shown in Figure 9., Mg variation in $Zn_{1-x}Mg_xO$ barriers would, again, produce a relevant impact on the magnitude of the tunnelling current, PVR and current-density peak-to-valley difference, indicating itself as an additional important parameter in prospective ZnO/ZnMgO THz QCL electron transport optimisation. The inset of Figure 9. shows that the value of around x=9% would produce a maximised value of the current-density peak-to-valley difference ΔJ in this particular structure.

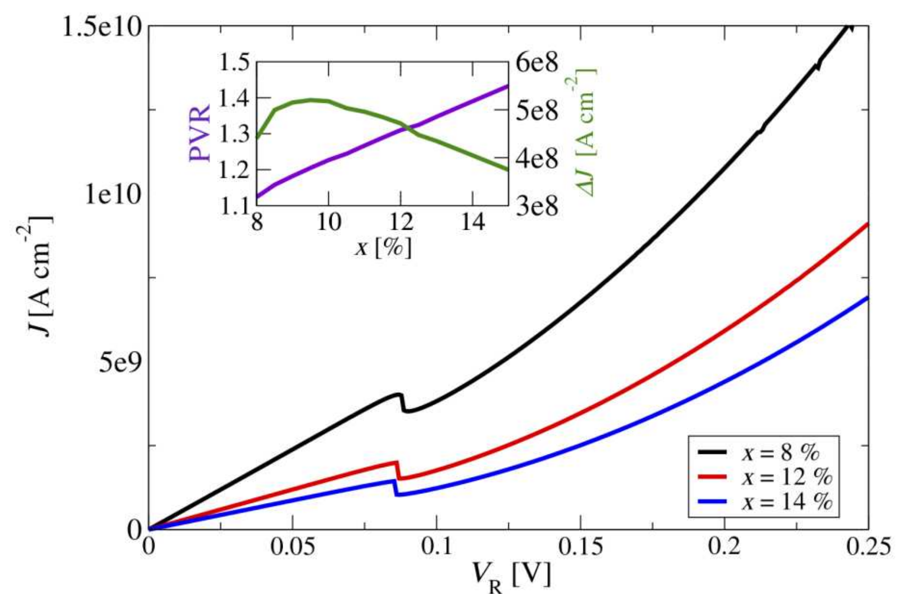

Figure 9. Current-density - voltage characteristics of non-polar *m*-plane $ZnO/Zn_{1-x}Mg_xO$ double-barrier resonant tunnelling structures. The optimal doping density in emitter/collector of 1×$\mathbf{10^{18}\ cm^{-3}}$ and barrier thickness of 1.3 nm were chosen, i.e. the nominal layer thicknesses barriers and quantum well of constituent epi-layers of the structure starting from the emitter in nm are 10/**1.3**/6/**1.3**/10 (thickness of quantum barriers is marked in bold). Inset shows the current-density peak-to-valley (PVR) ratio (left-hand y-axis) and current-density peak-to-valley difference (right-hand y-axis) at NDR; lattice temperature of T=300K is used in all simulations.

4. Conclusions

Experimental realisations of high electron-LO phonon resonance non-polar m-plane ZnO/ZnMgO-based intersubband heterostructures demand a comprehensive, but still simple theoretical model and analysis of the coherent tunnelling transport and intersubband optical absorption in these structures. We have modelled absorption in highly-doped MQW structures that mimic a QCL active region and discussed the importance of depolarization shift in ZnO/ZnMgO light absorbing/emitting ISBT structures. Furthermore, we have modelled current-voltage characteristics and analysed electron density distribution as a function of the voltage applied to the double-barrier resonant tunnelling structure. Calculations show that tunnelling current PVR is very sensitive both to small (monolayer) barrier thickness variation and to the percentage of Mg mole fraction changes, as well as to injector/collector doping density. This information would be useful

for optimising resonant tunnelling electron transport and injection efficiency in perspective structures like non-polar m-plane ZnO-based operating in the THz frequency range.

Author Contributions: Conceptualization, D.I., A.D., N.V., and J.R.; methodology, A.A., X.W., A.D. and N.V; software, A.A., X.W., N.S., N.V and A.D; validation, N.V., A.D., D.I and J.R.; formal analysis, A.D. and N.V, writing—original draft preparation, A.A., X.W. and N.S.; writing—review and editing, N.V., A.D., N.S., D.I. and J.R.; visualization, A.D.; supervision, N.V., A.D., D.I. and J.R; funding acquisition, J.R., D.I., N.V. All authors have read and agreed to the published version of the manuscript.

Funding: This work was supported by the "Multi-Scale Modeling of Terahertz Quantum Cascade Laser Active Regions", Multilateral scientific and technological cooperation in the Danube region 2020-2021, "DEMETRA: Development of high-performance mid-IR / THz quantum cascade lasers for advanced applications", Science Fund of the Republic of Serbia, Serbian Science and Diaspora Collaboration Programme: Knowledge Exchange Vouchers (Grant Number 6436915), European Cooperation in Science and Technology (COST) Action CA21159 PhoBioS, the Engineering and Physical Sciences Research Council (EPSRC) UK (Grant No. EP/T034246/1), Vlatacom Institute of High Technologies under project 178, the Ministry of Science, Technological Development and Innovation of the Republic of Serbia under contract numbers: 451-03-47/2023-01/20017 and 451-03-47/2023-01/200103, and by the Science Fund of the Republic of Serbia, 10504, Ultra-short pulsations from TERAhertz quantum cascade laser using passive mode-LOCKing with graphene saturable absorber - TERALOCK.

Data Availability Statement: Data will be made available on request.

Conflicts of Interest: The authors declare no conflict of interest.

Appendix A

U_{xc} is the local exchange-correlation potential expressed as [64]:

$$U_{xc}(z) = -\frac{e^4}{32\pi^2\hbar^2}\frac{m^*(z)}{\varepsilon^*(z)^2}\left(\frac{9\pi}{4}\right)^{\frac{1}{3}}\frac{2}{\pi r_s^*}\left[1 + 0.054 r_s^* log\left(1 + \frac{11.4}{r_s^*}\right)\right], \quad \text{(A1)}$$

where $\varepsilon^*(z)$ is the dielectric constant and r_s^* is the average distance between carriers scaled by the effective Bohr radius:

$$r_s^* = \sqrt[3]{\frac{3}{4\pi n(z)}}\frac{1}{a_B^*}, \quad \text{(A2)}$$

$$a_B^* = \frac{4\pi\varepsilon^*(z)\hbar^2}{m^*(z)e^2}, \quad \text{(A3)}$$

Appendix B

The Hamiltonian describing the intersubband plasmon can be written as [32]:

$$H_{plasmon} = \sum_{\alpha}\hbar\widetilde{\omega}_\alpha p_\alpha^\dagger p_\alpha + \frac{\hbar}{2}\sum_{\alpha\neq\beta}\Xi_{\alpha,\beta}(p_\alpha + p_\alpha^\dagger)(p_\beta + p_\beta^\dagger), \quad \text{(B1)}$$

where p_α is the destruction operator of the intersubband plasmons α, $\widetilde{\omega}_\alpha = \sqrt{\omega_\alpha^2 + \omega_{P\alpha}^2}$ is the plasma-shifted transition frequency where $\omega_{P\alpha}^2 = \frac{2e^2\Delta N_\alpha \omega_\alpha}{\hbar\varepsilon_0\varepsilon_s}S_{\alpha\alpha}$. The coupling due to dipole-dipole Coulomb interaction is described by the coupling strength $\Xi_{\alpha,\beta}$:

$$\Xi_{\alpha,\beta} = \frac{\omega_{P\alpha}\omega_{P\beta}}{2\sqrt{\widetilde{\omega}_{P\alpha}\widetilde{\omega}_{P\beta}}}C_{\alpha\beta}, \quad \text{(B2)}$$

$$C_{\alpha,\beta} = \frac{S_{\alpha\beta}}{\sqrt{S_{\alpha\alpha}S_{\beta\beta}}}, \quad (B3)$$

where $S_{\alpha\beta}$ is the characteristic length that depends on the overlap between micro-currents, given as:

$$S_{\alpha\beta} = \frac{1}{\hbar\omega_\alpha}\frac{1}{\hbar\omega_\beta}\left(\frac{\hbar^2}{2m^*}\right)^2 \int_{-\infty}^{+\infty} dz\xi_\alpha(z)\xi_\beta(z). \quad (B4)$$

Diagonal terms $S_{\alpha\alpha}$ refer to the interaction between dipoles associated with the same transition, while the $S_{\alpha\beta}$ are the dipoles belonging to different transitions. In the eq.(16) $\xi_\alpha(z)$ term is given by:

$$\xi_\alpha(z) \equiv \xi_{ij}(z) = \psi_i(z)\frac{\partial\psi_j(z)}{\partial z} - \psi_j(z)\frac{\partial\psi_i(z)}{\partial z}. \quad (B5)$$

The coupling between N intersubband plasmons leads to the multisubband plasmons due to Coulomb interaction. The new *N* frequency W_N can be calculated by diagonalizing the following $2N \times$ 2N matrix [32]:

$$M = \begin{bmatrix} I_1 & C_{12} & \dots & C_{1N} \\ C_{12} & I_2 & \dots & C_{2N} \\ \vdots & \vdots & \ddots & \vdots \\ C_{1N} & C_{2N} & \dots & I_N \end{bmatrix} \quad (B6)$$

$$M = \begin{bmatrix} \omega_\alpha & 0 \\ 0 & -\omega_\alpha \end{bmatrix}, \quad M = \begin{bmatrix} \Xi_{\alpha,\beta} & -\Xi_{\alpha,\beta} \\ \Xi_{\alpha,\beta} & -\Xi_{\alpha,\beta} \end{bmatrix}. \quad (B7)$$

Each new eigenmode of the system W_n is associated with the excitation of a multisubband plasmon, described by the operators:

$$P_n = \sum (a_{n\alpha}p_\alpha + b_{n\alpha}p_\alpha^\dagger), \quad (B8)$$

where components of the eigenvectors $V_n = (a_{n1}, b_{n1}, \dots, a_{nN}, b_{nN})^T$ satisfy the bosonic normalization condition:

$$\sum (|a_{n\alpha}|^2 - |b_{n\alpha}|^2) = 1. \quad (B9)$$

We can now write the Hamiltonian (S2.1) using multisubband plasmons modes as:

$$H_{plasmon} = \sum_n \hbar W_n P_n^\dagger P_n. \quad (B10)$$

The current density for n-th multisubband plasmon is written as:

$$J_n(z) = \frac{e\hbar}{2m^*\sqrt{S}} W_n \sum_\alpha \frac{\xi_\alpha(z)\sqrt{\Delta N_\alpha}}{\sqrt{\omega_\alpha\widetilde{\omega}_\alpha}}(a_{n\alpha} + b_{n\alpha})^{-1}. \quad (B11)$$

References

1. Faist, J. *Quantum Cascade Lasers*; EBSCO ebook academic collection; OUP Oxford, 2013; ISBN 9780198528241.
2. *Terahertz and Mid Infrared Radiation: Detection of Explosives and CBRN (Using Terahertz)*; Pereira, M.F., Shulika, O., Eds.; NATO Science for Peace and Security Series B: Physics and Biophysics; Springer Netherlands: Dordrecht, 2014; ISBN 978-94-017-8571-6.

3. Sirtori, C. Terahertz Race Heats Up. *Nat. Photonics* **2021**, *15*, 1–2, doi:10.1038/s41566-020-00740-4.
4. Williams, B.S. Terahertz Quantum-Cascade Lasers. *Nat. Photonics* **2007**, *1*, 517–525, doi:10.1038/nphoton.2007.166.
5. *Mid-Infrared and Terahertz Quantum Cascade Lasers*; Botez, D., Belkin, M.A., Eds.; Cambridge University Press, 2023; ISBN 9781108552066.
6. Pereira, M. Analytical Expressions for Numerical Characterization of Semiconductors per Comparison with Luminescence. *Materials (Basel).* **2017**, *11*, 2, doi:10.3390/ma11010002.
7. Oriaku, C.I.; Pereira, M.F. Analytical Solutions for Semiconductor Luminescence Including Coulomb Correlations with Applications to Dilute Bismides. *J. Opt. Soc. Am. B* **2017**, *34*, 321, doi:10.1364/JOSAB.34.000321.
8. Pereira, M.F.; Henneberger, K. Microscopic Theory for the Optical Properties of Coulomb-Correlated Semiconductors. *Phys. status solidi* **1998**, *206*, 477–491, doi:10.1002/(SICI)1521-3951(199803)206:1<477::AID-PSSB477>3.0.CO;2-5.
9. Pereira, M.F.; Zubelli, J.P.; Winge, D.; Wacker, A.; Rodrigues, A.S.; Anfertev, V.; Vaks, V. Theory and Measurements of Harmonic Generation in Semiconductor Superlattices with Applications in the 100 GHz to 1 THz Range. *Phys. Rev. B* **2017**, *96*, 045306, doi:10.1103/PhysRevB.96.045306.
10. Pereira, M.F.; Anfertev, V.; Shevchenko, Y.; Vaks, V. Giant Controllable Gigahertz to Terahertz Nonlinearities in Superlattices. *Sci. Rep.* **2020**, *10*, 15950, doi:10.1038/s41598-020-72746-5.
11. Vaks, V.; Anfertev, V.; Chernyaeva, M.; Domracheva, E.; Yablokov, A.; Maslennikova, A.; Zhelesnyak, A.; Baranov, A.; Schevchenko, Y.; Pereira, M.F. Sensing Nitriles with THz Spectroscopy of Urine Vapours from Cancers Patients Subject to Chemotherapy. *Sci. Rep.* **2022**, *12*, 18117, doi:10.1038/s41598-022-22783-z.
12. Pereira, M.F.; Anfertev, V.A.; Zubelli, J.P.; Vaks, V.L. Terahertz Generation by Gigahertz Multiplication in Superlattices. *J. Nanophotonics* **2017**, *11*, 1, doi:10.1117/1.JNP.11.046022.
13. Apostolakis, A.; Pereira, M.F. Potential and Limits of Superlattice Multipliers Coupled to Different Input Power Sources. **2019**, doi:10.1117/1.JNP.13.036017.
14. Apostolakis, A.; Pereira, M.F. Superlattice Nonlinearities for Gigahertz-Terahertz Generation in Harmonic Multipliers. *Nanophotonics* **2020**, *9*, 3941–3952, doi:10.1515/nanoph-2020-0155.
15. Apostolakis, A.; Pereira, M.F. Controlling the Harmonic Conversion Efficiency in Semiconductor Superlattices by Interface Roughness Design. *AIP Adv.* **2019**, *9*, doi:10.1063/1.5050917.
16. Pereira, M.F. Harmonic Generation in Biased Semiconductor Superlattices. *Nanomaterials* **2022**, *12*, 1504, doi:10.3390/nano12091504.
17. Hillbrand, J.; Matthieu Krüger, L.; Dal Cin, S.; Knötig, H.; Heidrich, J.; Maxwell Andrews, A.; Strasser, G.; Keller, U.; Schwarz, B. High-Speed Quantum Cascade Detector Characterized with a Mid-Infrared Femtosecond Oscillator. *Opt. Express* **2021**, *29*, 5774, doi:10.1364/OE.417976.
18. Zafar, H.; Pereira, M.F.; Kennedy, K.L.; Anjum, D.H. Fabrication-Tolerant and CMOS-Compatible Polarization Splitter and Rotator Based on a Compact Bent-Tapered Directional Coupler. *AIP Adv.* **2020**, *10*, doi:10.1063/5.0030638.
19. Zafar, H.; Zhai, Y.; Villegas, J.E.; Ravaux, F.; Kennedy, K.L.; Pereira, M.F.; Rasras, M.; Shamim, A.; Anjum, D.H. Compact Broadband (O, E, S, C, L & U Bands) Silicon TE-Pass Polarizer Based on Ridge Waveguide Adiabatic S-Bends. *Opt. Express* **2022**, *30*, 10087, doi:10.1364/OE.452823.
20. Zafar, H.; Paredes, B.; Taha, I.; Villegas, J.E.; Rasras, M.; Pereira, M.F. Compact and Broadband Adiabatically Bent Superlattice-Waveguides With Negligible Insertion Loss and Ultra-Low Crosstalk. *IEEE J. Sel. Top. Quantum Electron.* **2023**, *29*, 1–9, doi:10.1109/JSTQE.2023.3241617.
21. Zafar, H.; Paredes, B.; Villegas, J.; Rasras, M.; Pereira, M.F. O-Band TE- and TM-Mode Densely Packed Adiabatically Bent Waveguide Arrays on the Silicon-on-Insulator Platform. *Opt. Express* **2023**, *31*, 21389–21398, doi:10.1364/OE.493077.
22. Cardilli, M.C.; Dabbicco, M.; Mezzapesa, F.P.; Scamarcio, G. Linewidth Measurement of Mid Infrared Quantum Cascade

Laser by Optical Feedback Interferometry. *Appl. Phys. Lett.* **2016**, *108*, doi:10.1063/1.4940116. 544
23. Li, L.H.; Zhu, J.X.; Chen, L.; Davies, A.G.; Linfield, E.H. The MBE Growth and Optimization of High Performance Terahertz Frequency Quantum Cascade Lasers. *Opt. Express* **2015**, *23*, 2720, doi:10.1364/OE.23.002720. 545 546
24. Winge, D.O.; Franckié, M.; Verdozzi, C.; Wacker, A.; Pereira, M.F. Simple Electron-Electron Scattering in Non-Equilibrium Green's Function Simulations. *J. Phys. Conf. Ser.* **2016**, *696*, 012013, doi:10.1088/1742-6596/696/1/012013. 547 548
25. Leitenstorfer, A.; Moskalenko, A.S.; Kampfrath, T.; Kono, J.; Castro-Camus, E.; Peng, K.; Qureshi, N.; Turchinovich, D.; Tanaka, K.; Markelz, A.G.; et al. The 2023 Terahertz Science and Technology Roadmap. *J. Phys. D. Appl. Phys.* **2023**, *56*, 223001, doi:10.1088/1361-6463/acbe4c. 549 550 551
26. Wang, R.; Täschler, P.; Wang, Z.; Gini, E.; Beck, M.; Faist, J. Monolithic Integration of Mid-Infrared Quantum Cascade Lasers and Frequency Combs with Passive Waveguides. *ACS Photonics* **2022**, *9*, 426–431, doi:10.1021/acsphotonics.1c01767. 552 553
27. Dakhlaoui, H.; Nefzi, M. Enhancement of the Optical Absorption in MgZnO/ZnO Quantum Well under External Electric Field. *Optik (Stuttg).* **2018**, *157*, 1342–1349, doi:10.1016/j.ijleo.2017.12.107. 554 555
28. Jirauschek, C.; Kubis, T. Modeling Techniques for Quantum Cascade Lasers. *Appl. Phys. Rev.* **2014**, *1*, 011307, doi:10.1063/1.4863665. 556 557
29. Vukovic, N.; Radovanovic, J.; Milanovic, V.; Boiko, D.L. Numerical Study of Risken–Nummedal–Graham–Haken Instability in Mid-Infrared Fabry–Pérot Quantum Cascade Lasers. *Opt. Quantum Electron.* **2020**, *52*, 91, doi:10.1007/s11082-020-2210-4. 558 559 560
30. Isić, G.; Radovanović, J.; Milanović, V. Anisotropic Spin-Dependent Electron Tunneling in a Triple-Barrier Resonant Tunneling Diode. *J. Appl. Phys.* **2007**, *102*, 123704, doi:10.1063/1.2825401. 561 562
31. Ando, T.; Fowler, A.B.; Stern, F. Electronic Properties of Two-Dimensional Systems. *Rev. Mod. Phys.* **1982**, *54*, 437–672, doi:10.1103/RevModPhys.54.437. 563 564
32. Pegolotti, G.; Vasanelli, A.; Todorov, Y.; Sirtori, C. Quantum Model of Coupled Intersubband Plasmons. *Phys. Rev. B* **2014**, *90*, 035305, doi:10.1103/PhysRevB.90.035305. 565 566
33. Khalatpour, A.; Tam, M.C.; Addamane, S.J.; Reno, J.; Wasilewski, Z.; Hu, Q. Enhanced Operating Temperature in Terahertz Quantum Cascade Lasers Based on Direct Phonon Depopulation. *Appl. Phys. Lett.* **2023**, *122*, doi:10.1063/5.0144705. 567 568
34. Demić, A.; Ikonić, Z.; Dean, P.; Indjin, D. Dual Resonance Phonon–Photon–Phonon Terahertz Quantum-Cascade Laser: Physics of the Electron Transport and Temperature Performance Optimization. *Opt. Express* **2020**, *28*, 38788, doi:10.1364/OE.410014. 569 570 571
35. Demić, A.; Ikonić, Z.; Dean, P.; Indjin, D. Prospects of Temperature Performance Enhancement through Higher Resonant Phonon Transition Designs in GaAs-Based Terahertz Quantum-Cascade Lasers. *New J. Phys.* **2022**, *24*, 033047, doi:10.1088/1367-2630/ac5b41. 572 573 574
36. Pearton, S.; Ren, F. Advances in ZnO-Based Materials for Light Emitting Diodes. *Curr. Opin. Chem. Eng.* **2014**, *3*, 51–55, doi:10.1016/j.coche.2013.11.002. 575 576
37. Huang, J.; Yin, Z.; Zheng, Q. Applications of ZnO in Organic and Hybrid Solar Cells. *Energy Environ. Sci.* **2011**, *4*, 3861, doi:10.1039/c1ee01873f. 577 578
38. Ma, A.M.; Gupta, M.; Chowdhury, F.R.; Shen, M.; Bothe, K.; Shankar, K.; Tsui, Y.; Barlage, D.W. Zinc Oxide Thin Film Transistors with Schottky Source Barriers. *Solid. State. Electron.* **2012**, *76*, 104–108, doi:10.1016/j.sse.2012.05.005. 579 580
39. Di Russo, E.; Mancini, L.; Moyon, F.; Moldovan, S.; Houard, J.; Julien, F.H.; Tchernycheva, M.; Chauveau, J.M.; Hugues, M.; Da Costa, G.; et al. Three-Dimensional Atomic-Scale Investigation of ZnO-Mg x Zn 1−x O m-Plane Heterostructures. *Appl. Phys. Lett.* **2017**, *111*, 032108, doi:10.1063/1.4994659. 581 582 583
40. Pan, X.Q.H.; Guo, W.; Tian, W.; He, H.P.; Ye, Z.Z.; Gu, X.Q.; Schlom, D.G.; Pan, X.Q.H. Optical Properties of ZnO/Zn0.9Mg0.1O Multiple Quantum Wells Grown on (111) Si Using Buffer Assisted Pulsed-Laser Deposition. *J. Appl.* 584 585

Phys. **2010**, *107*, 033102, doi:10.1063/1.3266171. 586

41. Zhu, J.; Kuznetsov, A.Y.; Han, M.-S.; Park, Y.-S.; Ahn, H.-K.; Ju, J.-W.; Lee, I.-H. Structural and Optical Properties of ZnO⁄Mg0.1Zn0.9O Multiple Quantum Wells Grown on ZnO Substrates. *Appl. Phys. Lett.* **2007**, *90*, 211909, doi:10.1063/1.2742574. 587 588 589
42. Chen, H.R.; Tsai, C.Y.; Huang, Y.C.; Kuo, C.C.; Hsu, H.C.; Hsieh, W.F. Optical Properties of One- and Two-Dimensional Excitons in m -Plane ZnO/MgZnO Multiple Quantum Wells. *J. Phys. D. Appl. Phys.* **2016**, *49*, 095105, doi:10.1088/0022-3727/49/9/095105. 590 591 592
43. Mohammed Ali, M.J.; Chauveau, J.M.; Bretagnon, T. Anisotropic Optical Properties of a Homoepitaxial (Zn,Mg)O/ZnO Quantum Well Grown on a -plane ZnO Substrate. *Phys. status solidi c* **2016**, *13*, 598–601, doi:10.1002/pssc.201510238. 593 594
44. Chauveau, J.-M.; Laügt, M.; Vennegùes, P.; Teisseire, M.; Lo, B.; Deparis, C.; Morhain, C.; Vinter, B. Non-Polar a -Plane ZnMgO/ZnO Quantum Wells Grown by Molecular Beam Epitaxy. *Semicond. Sci. Technol.* **2008**, *23*, 035005, doi:10.1088/0268-1242/23/3/035005. 595 596 597
45. Chauveau, J.-M.; Teisseire, M.; Kim-Chauveau, H.; Deparis, C.; Morhain, C.; Vinter, B. Benefits of Homoepitaxy on the Properties of Nonpolar (Zn,Mg)O/ZnO Quantum Wells on a-Plane ZnO Substrates. *Appl. Phys. Lett.* **2010**, *97*, 081903, doi:10.1063/1.3481078. 598 599 600
46. Meng, B.; Hinkov, B.; Biavan, N.M.L.; Hoang, H.T.; Lefebvre, D.; Hugues, M.; Stark, D.; Franckié, M.; Torres-Pardo, A.; Tamayo-Arriola, J.; et al. Terahertz Intersubband Electroluminescence from Nonpolar M-Plane ZnO Quantum Cascade Structures. *ACS Photonics* **2021**, *8*, 343–349, doi:10.1021/acsphotonics.0c01641. 601 602 603
47. Le Biavan, N.; Hugues, M.; Montes Bajo, M.; Tamayo-Arriola, J.; Jollivet, A.; Lefebvre, D.; Cordier, Y.; Vinter, B.; Julien, F.-H.; Hierro, A.; et al. Homoepitaxy of Non-Polar ZnO/(Zn,Mg)O Multi-Quantum Wells: From a Precise Growth Control to the Observation of Intersubband Transitions. *Appl. Phys. Lett.* **2017**, *111*, doi:10.1063/1.5003146. 604 605 606
48. Sirkeli, V.P.; Vatavu, S.A.; Yilmazoglu, O.; Preu, S.; Hartnagel, H.L. Negative Differential Resistance in ZnO-Based Resonant Tunneling Diodes. In Proceedings of the 2019 44th International Conference on Infrared, Millimeter, and Terahertz Waves (IRMMW-THz); IEEE, September 2019; pp. 1–2. 607 608 609
49. Liu, D. Theoretical Calculations of THz Intersubband Absorption in Step Quantum Well Structures Based on MgZnO/ZnO Materials at 77 K. *Opt. Quantum Electron.* **2023**, *55*, 1038, doi:10.1007/s11082-023-05247-0. 610 611
50. Janotti, A.; Van de Walle, C.G. Fundamentals of Zinc Oxide as a Semiconductor. *Reports Prog. Phys.* **2009**, *72*, 126501, doi:10.1088/0034-4885/72/12/126501. 612 613
51. Ekenberg, U. Enhancement of Nonparabolicity Effects in a Quantum Well. *Phys. Rev. B* **1987**, *36*, 6152–6155, doi:10.1103/PhysRevB.36.6152. 614 615
52. Sirtori, C.; Capasso, F.; Faist, J.; Scandolo, S. Nonparabolicity and a Sum Rule Associated with Bound-to-Bound and Bound-to-Continuum Intersubband Transitions in Quantum Wells. *Phys. Rev. B* **1994**, *50*, 8663–8674, doi:10.1103/PhysRevB.50.8663. 616 617 618
53. Chang, L.L.; Esaki, L.; Tsu, R. Resonant Tunneling in Semiconductor Double Barriers. *Appl. Phys. Lett.* **1974**, *24*, 593–595, doi:10.1063/1.1655067. 619 620
54. Mizuta, H.; Tanoue, T. *The Physics and Applications of Resonant Tunnelling Diodes*; Cambridge University Press, 1995; ISBN 9780521432184. 621 622
55. Sakr, S.; Warde, E.; Tchernycheva, M.; Julien, F.H. Ballistic Transport in GaN/AlGaN Resonant Tunneling Diodes. *J. Appl. Phys.* **2011**, *109*, doi:10.1063/1.3533975. 623 624
56. Indjin, M.; Griffiths, J. Coherent Electron Quantum Transport in In0.53Ga0.47As/GaA0.51Sb0.49 Double Barrier Resonant Tunnelling Structures. *Opt. Quantum Electron.* **2020**, *52*, 265, doi:10.1007/s11082-020-02359-9. 625 626
57. Blakemore, J.S. Semiconducting and Other Major Properties of Gallium Arsenide. *J. Appl. Phys.* **1982**, *53*, R123–R181, 627

doi:10.1063/1.331665. 628
58. Montes Bajo, M.; Chauveau, J.-M.; Vasanelli, A.; Delteil, A.; Todorov, Y.; Sirtori, C.; Hierro, A. Perspectives and Opportunities with Multisubband Plasmonics. *J. Appl. Phys.* **2023**, *134*, doi:10.1063/5.0152527. 629 630
59. Ribeiro, S.; Vasanelli, A.; Todorov, Y.; Sirtori, C. Quantum Theory of Multisubband Plasmon– Phonon Coupling. *Photonics* **2020**, *7*, 19, doi:10.3390/photonics7010019. 631 632
60. Le Biavan, N. Toward a Zinc Oxide Based Quantum Cascade Laser, COMUE Université Côte d'Azur (2015 - 2019), 2019. 633
61. Meng, B.; Tamayo-Arriola, J.; Le Biavan, N.; Montes Bajo, M.; Torres-Pardo, A.; Hugues, M.; Lefebvre, D.; Hierro, A.; Chauveau, J.M.; Faist, J. Observation of Intersubband Absorption in Zn O Coupled Quantum Wells. *Phys. Rev. Appl.* **2019**, *12*, 054007, doi:10.1103/PhysRevApplied.12.054007. 634 635 636
62. Atić, A.; Vuković, N.; Radovanović, J. Calculation of Intersubband Absorption in ZnO/ZnMgO Asymmetric Double Quantum Wells. *Opt. Quantum Electron.* **2022**, *54*, 810, doi:10.1007/s11082-022-04170-0. 637 638
63. Ayoub, I.; Kumar, V.; Abolhassani, R.; Sehgal, R.; Sharma, V.; Sehgal, R.; Swart, H.C.; Mishra, Y.K. Advances in ZnO: Manipulation of Defects for Enhancing Their Technological Potentials. *Nanotechnol. Rev.* **2022**, *11*, 575–619, doi:10.1515/ntrev-2022-0035. 639 640 641
64. Liu, D. Intersubband Optical Absorption in ZnO/MgZnO Triple Quantum Well Structures. *Appl. Phys. B* **2022**, *128*, 74, doi:10.1007/s00340-022-07799-7. 642 643

644

Disclaimer/Publisher's Note: The statements, opinions and data contained in all publications are solely those of the individual author(s) and contributor(s) and not of MDPI and/or the editor(s). MDPI and/or the editor(s) disclaim responsibility for any injury to people or property resulting from any ideas, methods, instructions or products referred to in the content. 645 646 647